

Contents lists available at ScienceDirect

# Acta Materialia

journal homepage: www.elsevier.com/locate/actamat



# Full length article



# Design of polycrystalline metallic alloys under multi-scale uncertainty by connecting atomistic to meso-scale properties

Md Maruf Billah, Pinar Acar

Department of Mechanical Engineering, Virginia Tech, Blacksburg, VA 24061, USA

#### ARTICLE INFO

# Keywords: Uncertainty quantification and propagation Binary metal-metal alloy Molecular dynamics Mechanical properties Microstructure design optimization

#### ABSTRACT

Uncertainty quantification plays a pivotal role in advancing the development of reliable and high-performance material designs via multiscale materials modeling. This study focuses on modeling the uncertainty of meso-scale mechanical properties, e.g. modulus of elasticity and yield strength of Ti-7Al, by incorporating the inherent randomness of substitutional atoms of the alloy and its microstructural texture. A molecular dynamics approach is employed to probe the epistemic uncertainty of single-crystal properties. Moreover, the aleatoric uncertainty is quantified using the experimental microstructural texture data of a previous investigation. The propagation of the epistemic and aleatoric uncertainty on the homogenized properties is investigated using an analytical uncertainty quantification method. Subsequently, the Ti-7Al alloy microstructures are designed to improve meso-scale mechanical properties under uncertainty by integrating the analytical method into the optimization scheme

# 1. Introduction

Multi-scale computational approaches provide a pathway for predicting and comprehending the mechanical, thermal, electrical, chemical, and optical properties of various material systems. A significant portion of these methods relies heavily on molecular dynamics (MD) simulations, which originated in the late 1950s [1]. Moreover, the introduction of the Integrated Computational Materials Engineering (ICME) paradigm has prompted a substantial focus on developing multi-scale computational models. These models are designed to capture the intricate connection between material response and the foundational microstructure [2]. Essential parameters for these material models are derived from the homogenization of single-crystal properties over a representative volume element (RVE) that can be estimated via experiments. However, microstructures inherently possess stochastic characteristics. To elaborate, specimens produced through identical manufacturing processes exhibit variations in microstructure, both within a single specimen and across all specimens. A foundational aspect of ICME is uncertainty quantification (UQ), entailing the creation of mathematical tools to assess the impact of microstructural stochasticity on the anticipated engineering properties [3]. There are several UQ methods to determine the uncertainty of homogenized microstructural properties due to the fluctuations of its parameters, including spectral

decomposition [4], Monte Carlo simulation [5–8], stochastic collocation [9], Kriging [10], and polynomial chaos expansion [11,12]. This present study focuses on quantifying the uncertainty of single-crystal properties (epistemic uncertainty) of Ti-7Al alloy using MD simulations and its propagation on microstructural properties. In addition, this study models the measured aleatoric uncertainty of microstructural texture using a finite element discretized form of the orientation distribution function. This investigation marks a pioneering endeavor in designing microstructures using an analytical UQ method to aim for the exact solution, integrating single crystal-level epistemic uncertainty arising from the randomness of substitutional atoms with microstructure-level aleatoric uncertainty stemming from the inevitable stochastic variation of the texture.

At present, approximately half of the global titanium production is allocated to the aerospace sector [13–15]. Titanium alloys are primarily recommended due to their commendable specific compatibility of modulus, greater cyclic fatigue resistance, and resistance against corrosion [16]. A persistent concern revolves around the behavior of  $\alpha/\beta$  titanium alloys under cold dwell cyclic fatigue conditions characterized by cyclic loading with pauses at normal temperature. The majority of commercially employed titanium alloys incorporate approximately 6 wt. % aluminum [17]. Few uncertainty studies on  $\alpha/\beta$  titanium alloys have been conducted previously, e.g. Worsnop et al. [18] examined crystallographic ordering tendencies during aging at 550 °C in both

<sup>\*</sup> Corresponding author.

E-mail address: pacar@vt.edu (P. Acar).

Nomenclature		$m^{\alpha}$	Mass of the atoms
		R	Universal gas constant
Α	Orientation distribution function (ODF)	$r_{\alpha\beta}$	Atomic distance between $\alpha$ and $\beta$
$A_c$	Arrhenius constant	$r_{\rm e}$	Equilibrium nearest-neighbor distance
В	Bulk modulus	$\mathbf{v}^{\alpha}$	Velocity of the atoms
C <sub>max</sub> & C <sub>min</sub> Maximum and minimum values of the screening range		α&β	Atomic indices
$E_a$	Activation energy	μ	Mean of any variable
$E_c$	Cohesive energy	$\rho_o$	Ratio between atomic electron density scaling factor
$f_{\alpha\beta}$	Atomic force between $\alpha$ and $\beta$	$\Sigma^2$	Variance of any variable
$F_{x}$	Cumulative distribution function	χ(r)	Orientation dependent single-crystal property
$f_x$	Probability density function (PDF)	$\Omega^{\alpha}$	Volume of atom $\alpha$
$J_n$	Jacobian determinant of the n <sup>th</sup> element		

# binary Ti-Al and Ti-Sn alloys.

Comprehensive characterization of the  $\alpha$ -phase microstructures was conducted using advanced techniques, such as transmission electron microscopy, scanning electron microscope, and low-angle X-ray scattering with coupling tensile testing. This multifaceted approach aimed to re-evaluate the property trade-offs inherent in each alloy system. Ding et al. [19] conducted an extensive investigation utilizing molecular dynamics along with cohesive finite element method to analyze crack propagation in B2-NiAl alloy. Their study employed a cohesive element model incorporating material input parameters derived from MD simulations, aiming to comprehend both micro and macro crack propagation mechanisms. An investigation by Acar et al. [20] focused on the inverse problem of discerning microstructural stochasticity in light of fluctuations in meso-scale material properties. This was achieved through the creation of an analytical UQ model, denoted as 'AUQLin'. Another study was conducted to ascertain the parameters of slip systems inherent in Ti-Al alloys, specifically Ti-7Al and Ti-0Al, by Acar et al. [21]. This study involved the analysis of the experimental results of tension and compression, focusing on the true stress-true strain curves of Ti-7Al and Ti-0Al. The microstructure was meticulously characterized by utilizing a rate-independent single-crystal constitutive model and the Orientation Distribution Function (ODF) approach, and the UQ formulation was employed for a thorough investigation of crystal plasticity. However, the optimal microstructure designs across various challenges are also notably influenced by epistemic uncertainty related to the variations of the parameters and predictions of numerical models [22]. Tran et al. [23] conducted a study examining the utilization of multi-level sampling techniques, namely multi-level Monte Carlo (MLMC) and multi-index Monte Carlo (MIMC) to examine the effects of microstructural variations in polycrystalline materials on the forecasts of homogenized material properties. Thillaithevan et al. [24] proposed a methodology to integrate material uncertainty arising from manufacturing defects in additive manufacturing into a functionally graded lattice optimization framework. This framework introduced a perturbation parameter to modify the design variables of microstructures, accommodating a wide range of uncertain material properties.

In the exploration of simulating the inherent stochasticity within material systems, there has been an adequate gap in addressing the epistemic uncertainty because of the 'lack of knowledge.' Specifically, the examination of uncertainty stemming from computational models remains significantly under-explored within the realm of computational modeling and microstructure design. Hence, the fluctuations are regarded as inherent uncertainties in the modeling process, when determining the mechanical characteristics of the Ti-7Al alloy [25–27]. The present study focuses on quantifying variations of mechanical properties under the uncertainty of single-crystal properties arising from the randomness of substitutional atoms and microstructural texture as a result of the fluctuations during processing. The classical atomistic approach is employed to determine the epistemic uncertainty of single-crystal mechanical properties (Young's modulus and yield

strength) of Ti-7Al alloy where the force-field is described by the second nearest-neighbor modified embedded atom method (2NN MEAM). Next, a finite element discretization-based homogenization approach is used to obtain the volume-averaged (meso-scale) properties of microstructures with consideration of previously mentioned stochastic single-crystal properties, and a stochastic representation of the microstructural texture descriptor, ODF. The aleatoric uncertainty related to ODFs arises from texture variations observed among specimens undergoing identical processes. This investigation was performed in our prior research [3], where measurements were conducted on various beta-forged Ti-7Al samples subjected to identical compression and annealing procedures. These measurements were obtained from diverse regions within the samples. Probability distributions of the pole figures were derived from these scans, revealing a predominantly Gaussian distribution pattern. Furthermore, the present work performs microstructure design under uncertainty to obtain optimum meso-scale properties by integrating the analytical UQ approach, providing the exact solution to the probability distribution representations of properties. Finally, the study is extended to meso-scale properties involving a non-linear relationship with the underlying microstructural texture using the transformation of random variables approach within the analytical UQ framework.

The organization of the paper is as follows: Section 2 discusses the mathematical methodology behind the computation of single crystal stress-strain behavior and homogenized microstructure properties with associated uncertainty quantification and propagation. Following this, Section 3 elaborates on the resultant outcomes and proposes solutions for microstructure design. Finally, Section 4 upholds the comprehensive conclusions drawn from this study.

#### 2. Methodology

# 2.1. Computation of single-crystal properties

The alloy under investigation is Ti-7wt %Al (Ti-7Al), a recognized α-Ti binary alloy distinguished by its hexagonal close-packed (HCP) crystal structure. In this particular investigation, the lattice constants of a = b = 2.932 Å and c = 4.684 Å are employed to construct the unit cell of Ti-7Al [28]. Afterward, ~12 % Al atoms are randomly located on the crystal to ensure a perfectly substitutional alloy. The consequent alloy structure takes the form of a cuboid, as depicted in Fig. 1, with final dimensions of 80.63  $\mathring{A} \times 85.49 \ \mathring{A} \times 81.97 \ \mathring{A}$ . Utilizing a consistent approach, 160 different samples are prepared for MD studies by keeping the indistinguishable dimension while introducing random variations in the positions of Al atoms on the  $\alpha$ -structure. The force field of the atoms of the single-crystal structure has been defined by 2NN MEAM potential parameters [29]. MEAM represents a reactive semiempirical many-body potential grounded in density functional theory. Since its inception in 1992, the MEAM potential has proven effective in computing the physical characteristics of numerous crystal structures, including

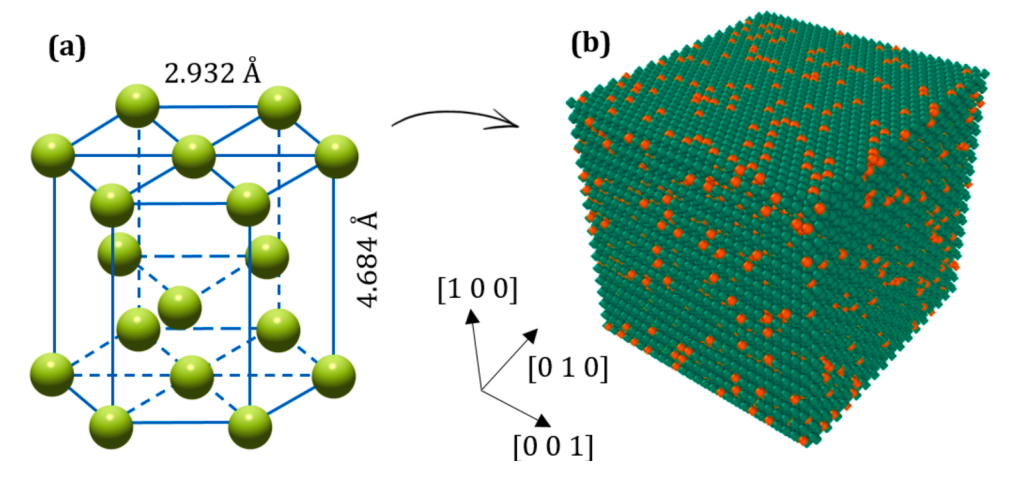


Fig. 1. (a) Unit cell of α-Titanium and (b) The single-crystal structure of Ti-7Al, green and orange atoms represent Titanium and Aluminum, respectively.

face-centered cubic (FCC), body-centered cubic (BCC), HCP, and diamond cubic, within unary, binary, ternary, and more complex metallic systems [30–34].

$$E = \sum_{i} \left( F(\overline{\rho}_i) + \frac{1}{2} \sum_{j \neq 1} S(r_{ij}) \varphi(r_{ij}) \right)$$
 (1)

The fundamental expression for total energy for any atom of i can be described as the summation of the embedding function and traditional pair-interaction of atoms i and j which has been upheld in Eq. (1); where  $\overline{\rho}_i$ ,  $r_{ij}$ ,  $S(r_{ij})$ , and  $\varphi(r_{ij})$  represent background electron density, distance, screening function, and interaction potential respectively between atom i and j. Interested readers are referred to Refs. [29,30] for more details about the inter-atomic potential of the metallic-alloy. The 2NN MEAM potential parameters of  $\alpha$  binary Ti and Al system are listed in Table 1.

In each computation, the periodic boundary conditions are applied to all three directions of the samples, effectively diminishing the influence of the boundary/edge effect on the structure. Before subjecting the structures to a constant strain rate, a comprehensive energy minimization process is undertaken to achieve equilibrium among all atoms. The minimization involves a two-stage combined optimization method. First and foremost, the NVT (stands for the number of atoms, volume, and temperature of the structure) canonical ensemble is conducted for a total time of 5 picoseconds. This is aimed at the determination of the positions and velocities of each atom using non-Hamiltonian equations in the Nose-Hoover method at every time step. Following this, the simulation is extended for an additional 50 picoseconds, utilizing the NPT (stands for the number of atoms, pressure, and temperature of the structure) isothermal-isobaric ensemble where the objective of this phase is to resolve the kinematics parameters, such as linear/angular positions,

Table 1
2NN MEAM parameters of Ti-7Al [29].

	Ti	Al	Ti-Al
$E_c$ (eV)	4.87	3.36	-0.26
$r_e$ (Å)	2.92	2.86	2.8
B (10 <sup>11</sup> Pa)	1.10	0.794	1.426
d	0.0	0.05	$0.5d^{\mathrm{Ti}} + 0.5d^{\mathrm{A}l}$
C <sub>min</sub> (Ti–Al–Ti)	1.00	0.49	1.3
$C_{min}$ (Al-Ti-Al)			$0.49(=C_{min}^{Al})$
C <sub>min</sub> (Ti–Ti–Al)			0.46
C <sub>min</sub> (Ti– Al–Al)			$0.72 (= [0.5 \sqrt{C_{min}^{Ti}} + 0.5 \sqrt{C_{min}^{Al}}]^2)$
C <sub>max</sub> (Ti-Al -Ti)	1.44	2.80	2.8
$C_{max}$ (Al-Ti-Al)			1.44
C <sub>max</sub> (Ti-Ti-Al)			1.44
$C_{max}$ (Ti–Al –Al)			2.88
$\rho_o$	1	1	$1(\ = \rho_0^{Al} \ / \rho_0^{Ti})$

orientations, and velocities of all atoms at every time step. The temporal resolution for both ensembles is set at 0.001 ps. Upon finishing these two successive computation steps, the sample nano-structures achieve a state of near equilibrium concerning pressure and temperature.

The NPT ensemble is employed to keep constant temperature and pressure in conjunction with the imposition of uniaxial deformation along the [1 0 0] direction, featuring a specified strain rate of  $10^{10} \, \mathrm{s}^{-1}$  at a temperature of 300 K. The assessment of structural stress corresponding to the applied strain relies on the application of the virial stress theorem [35]. Mechanical stress ( $\sigma^a_{ij}$ ), as quantified by Eq. (2), derived from the virial theorem, involves the computation of stress through a functional derivative of the atomistic system's free energy concerning the deformation tensor. In this equation, the symbols i and j denote the axes of the coordinate system by taking values 1, 2, and 3. The atomic volume, mass, velocity components of  $\alpha$  atom in i and j directions, interatomic force, and magnitude of distance vector between  $\alpha$  and  $\beta$  atoms are represented by  $\Omega^{\alpha}$ ,  $m^{\alpha}$ ,  $\nu^{\alpha}_i$ ,  $\nu^{\alpha}_j$ ,  $f^{i}_{\alpha\beta}$  and  $r^{i}_{\alpha\beta}$ . According to the sign convention, a positive stress indicates attraction between particles, while a negative stress signifies repulsion.

$$\sigma_{ij}^{a} = \frac{1}{\Omega^{a}} \left( \frac{1}{2} m^{a} \nu_{i}^{a} \nu_{j}^{a} + \sum_{\beta=1}^{n} r_{\alpha\beta}^{i} f_{\alpha\beta}^{j} \right) \tag{2}$$

# 2.2. Computation of microstructure properties

The current study models the crystallographic texture of the Ti-7Al microstructure by utilizing the ODFs. This function measures the volume densities of distinct crystallographic orientations within a polycrystalline material and can be used as the parameter to obtain the homogenized properties. Parametrization methods like Rodrigues parameters [36–39] and Euler angles [40–44] are employed to define the ODFs. Specifically, a local finite element discretization method for ODFs has been applied within the framework of Rodrigues orientation space to compute the homogenized properties in this study. The computation of homogenized properties involves an integration across the fundamental region  $(\Omega)$ , taking into account lattice rotation denoted as R. By leveraging the Rodrigues orientation vector  $(\mathbf{r})$ , the expression of R is described in Eq. (3).

$$R = \frac{1}{1+rr} (I(1-rr) + 2(r \otimes r + I \times r))$$
(3)

The definition of the ODF is articulated in Eq. (4), with regard to crystal volume densities that must satisfy a volume normalization constraint [45–48]. Upon employing crystal symmetries, the polycrystalline material's orientation space can be simplified into a more concise subset recognized as the fundamental region illustrated in Fig. 2.

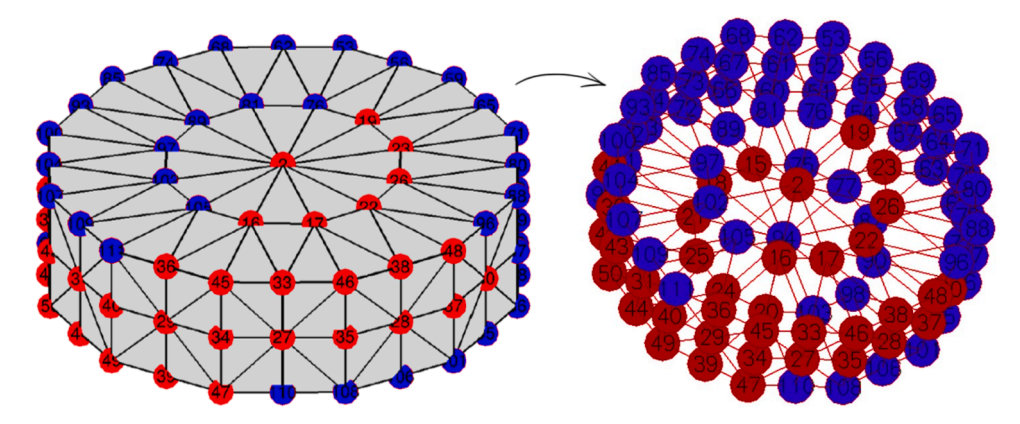


**Fig. 2.** Illustration of the finite element discretization approach for the ODFs within the Rodrigues fundamental region for hexagonal crystal ( $\alpha$  Ti-7Al) symmetry, highlighting the nodes arrangement of the k = 50 independent ODFs in red color.

The discretization of this fundamental region employs the local finite element approach featuring N number of independent nodes and  $N_{elm}$  number of finite elements, accompanied by  $N_{int}$  number of integration points per element. Rodrigues orientation space can be applied for discretization, which proves preferable because of its ability to yield regular geometries [49–52]. Every nodal point within the fundamental region mesh corresponds to a distinct ODF value intricately connected with the volume density of the associated crystallographic orientation. This concise representation facilitates the determination of volume-averaged (meso-scale) material properties of microstructure by considering the ODF values at nodal points.

$$\int_{\Omega} A dv = \sum_{n=1}^{N_{elm}} \sum_{m=1}^{N_{int}} A(\mathbf{r}_m) \ w_m |J_n| \frac{1}{(1 + \mathbf{r}_m \cdot \mathbf{r}_m)^2} = 1$$
 (4)

$$\langle \chi \rangle = \int_{\Omega} \chi(\mathbf{r}) A(\mathbf{r}) dv = \sum_{n=1}^{N_{elm}} \sum_{m=1}^{N_{int}} \chi(\mathbf{r_m}) A(\mathbf{r_m}) w_m |J_n| \frac{1}{(1 + \mathbf{r_m} \cdot \mathbf{r_m})^2}$$
(5)

Initially, all ODFs defined within the fundamental region must adhere to the constraint of volume normalization (unit volume-fraction) as delineated in Eq. (4) which can be represented as a linear equation  $q^TA=1$ , in terms of the ODF values defined at nodal points. By utilizing the same method, the orientation-dependent homogenized (volume-averaged) material property, denoted as  $\langle \chi \rangle$ , can be computed using single-crystal property values  $(\chi)$  alongside the nodal point ODFs as shown in Eq. (5). This formulation can also be represented as a linear equation  $<\chi>=p^TA$ , in terms of the ODF values at nodal points where p shows the property tensor with  $p_i=\chi_i(r_i)w_i|J_i|\frac{1}{(1+r_i,r_i)^2}$ .

# 2.3. Modeling of uncertainty propagation

First, the uncertainty propagation on the single-crystal properties is considered because of the randomness of the substitutional atoms in the  $\alpha$ -Ti structure. It is primarily defined that the reason for the variations of the mechanical properties is the locational variation of Al on the alloy, which has been examined through a mathematical expression. This variation is classified as epistemic uncertainty. The evaluated elastic modulus and yield strength frequency distributions are shown to agree with the cumulative distribution function of a Gaussian distribution given by Eq. (6),  $F:\mathbb{R} \to [0,1]$  that satisfies  $\lim_{x\to -\infty} F(x) = 0$  and  $\lim_{x\to \infty} F(x) = 0$ 

$$F_x(x) = \frac{1}{2} \left[ 1 + \operatorname{erf}\left(\frac{x - \mu}{\Sigma \sqrt{2}}\right) \right]$$
 (6)

Subsequently, the uncertainty propagation on microstructural properties is examined with the consideration of stochastic texture and single-crystal properties. The vector of ODF mean values,  $\mu_A$  is formed at

k independent nodes, assuming that these ODFs agree with a multivariate Gaussian distribution. This assumption is derived based on the experimental data of 150 microstructure data samples of the Ti-7Al alloy processed with the same parameters, as reported by our group in the previous work [3]. Next, the mean and variance of the homogenized properties (i.e. elastic modulus and yield strength) of the microstructure are determined by Eqs. (7) and (8) where a generic notation, Z is used to represent both homogenized elastic modulus and yield strength parameters. However, there is no specific correlation between the single-crystal property values and the ODFs that exhibits the null correlation coefficient ( $\rho$ =0). On the other hand, the normalization constraint should be expanded to another variance equation, which can be written as  $Q^2\Sigma_A^2 = 0$ , where  $Q = q^T$ . The formation of the set of equations, given in Eq. (9), arises from the incorporation of the uncertainty and the corresponding two new constraints for the variance.

$$\mu_Z = \mu_P \mu_A \tag{7}$$

$$\Sigma_Z^2 = \Sigma_P^2 \mu_A^2 + \mu_P^2 \Sigma_A^2 + \Sigma_P^2 \Sigma_A^2 + 2\rho(\mu_P \mu_A)(\Sigma_P \Sigma_A) + \rho^2 (\Sigma_P^2 \Sigma_A^2)$$
 (8)

$$\begin{bmatrix} 1 \\ \mu_Z \\ \mathbf{\Sigma}_Z^2 \\ 0 \end{bmatrix} = \begin{bmatrix} \mathbf{Q} & 0 & 0 \\ \mu_P & 0 & 0 \\ 0 & \mathbf{\Sigma}_P^2 & \mu_P^2 + \mathbf{\Sigma}_P^2 \\ 0 & 0 & \mathbf{Q}^2 \end{bmatrix} \begin{bmatrix} \mu_A \\ \mu_A^2 \\ \mathbf{\Sigma}_A^2 \end{bmatrix}$$
(9)

#### 3. Results and discussions

# 3.1. Uncertainty of single-crystal properties

Uniaxial tension ( $\sigma_{11} \neq 0$ ,  $\sigma_{22} = \sigma_{33} = 0$ ) is applied to 160 samples of different single crystal designs to carry out the mechanical properties, such as elastic modulus and yield strength for the direction perpendicular to zigzag and armchair directions. Prior to going through the NPT tension process, the samples are completely stable in terms of temperature and pressure; 5 ps of NVT ensemble has been employed to settle down the temperature at 300 K and successively 50 ps of NPT ensemble relaxed the samples to keep the zero pressure, which has been illustrated in Fig. 3. As a result, the samples are totally prepared for examining any further computation. Following the initiation of uniaxial stress at 55 ps, the sample began accumulating strain energy, causing the overall energy curve to steadily ascend until reaching its peak. It is noteworthy that the peaks of the stress and energy curves don't align simultaneously. The stress curve reaches its pinnacle at ultimate strength, while the energy curve continues to rise until the fracture of the sample occurred. At a constant strain rate of  $10^{10}~{\rm s}^{-1}$  (=  $\dot{\varepsilon}_{11}=d\varepsilon_{11}/dt$ ), the main stress-strain simulation is conducted in [1 0 0] direction ( $\ddot{\epsilon}_{11}=0,\,\epsilon_{22}\neq0,\,\epsilon_{33}\neq0$ ) at

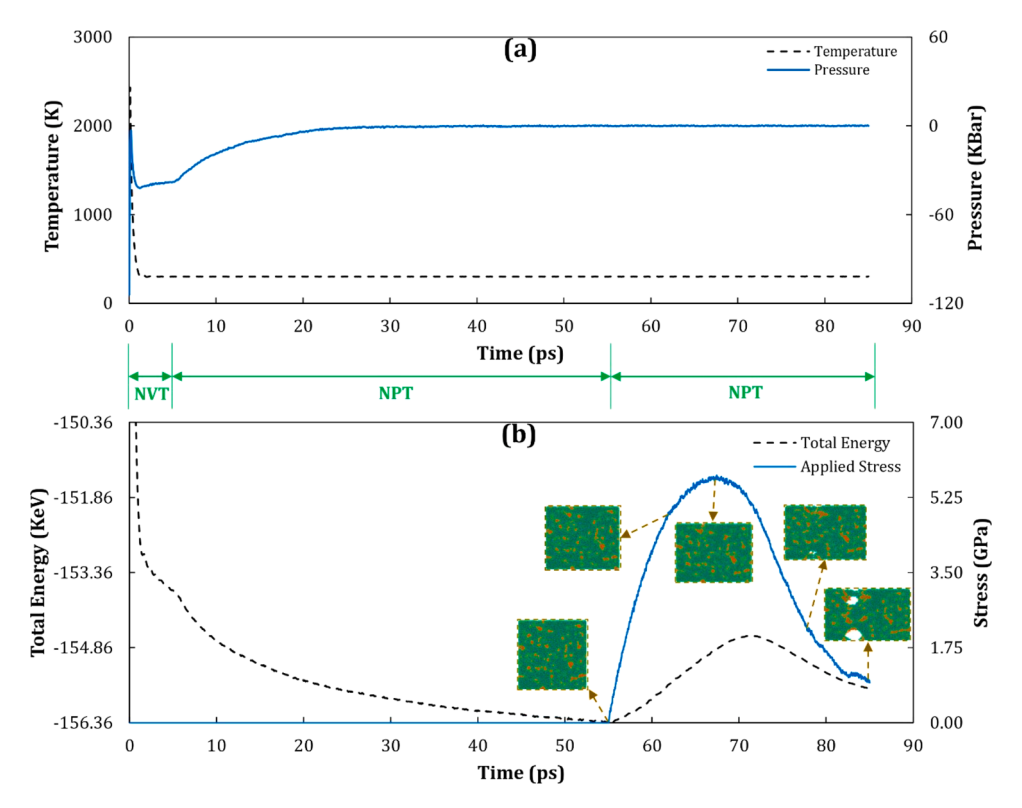


Fig. 3. (a) Temperature and pressure responses, (b) Total energy and applied stress along [1 0 0] direction with respect to the time. The (0 1 0) plane view of a random sample on loading has been illustrated at the stress curve.

previously achieved constant pressure and temperature through next 30 ps. The stress-strain curves of all 160 samples can be found in the Appendix. The modulus of elasticity can be evaluated from the slope of the linear region of stress versus strain curve; alternatively,  $E_{11} = \sigma_{11}/\varepsilon_{11}$ where  $\dot{\sigma}_{11} = d\sigma_{11}/dt$  on the stress versus time response curve. The examined elastic modulus  $(E_{11})$  values of all samples are within the limit of 118.537-129.777 GPa with a mean and standard deviation of 123.344 GPa and 2.447 GPa, respectively after fitting the cumulative Gaussian/normal frequency distribution as shown in Fig. 4(a). On the other hand, the yield strength of all samples has been measured from the stress-strain response by applying the conventional offset rule. This investigation carries out the yield strength of Ti-7Al within the range of 5.167-5.426 GPa which is further utilized in Eq. (6) in order to determine the mean and standard deviation as illustrated in Fig. 4(b); reported as 5.314 GPa and 47.2 MPa, respectively. The comprehensive observation from these results can be noted that the frequency distributions closely matched with the normal distribution where the elastic modulus curves are more aligned compared to the yield strength curves.

# 3.1.1. Yield strength at low strain rate

The investigation of stress-strain characteristics is conducted under elevated strain rates, a constraint inherent in the MD simulation. As a result, the recorded yield and ultimate strength values for all samples are notably higher. Nevertheless, to align the simulated yield strength with the ASTM standard strain rate of 0.015/min, an Arrhenius correlation [53], as described in Eq. (10), is utilized to scale down the yield strength. Arrhenius correlation provides a relation between flow stress ( $\sigma$ ) and strain rate  $(\varepsilon)$  at a given temperature. More specifically, the strain rate sensitivity (m) serves as a measure of how a material responds to variations in strain rate within the plastic deformation region where materials perform liquid-like behavior. This sensitivity parameter, denoted by Eq. (11), has been transformed into a linear expression by applying the natural logarithm to both sides of the Arrhenius equation. Next, Eq. (12) has been employed to ascertain the strain rate sensitivity of Ti-7Al, involving four stress-strain simulations conducted at distinct strain rates  $5 \times 10^{10}$ ,  $1 \times 10^{10}$ ,  $2 \times 10^9$  and  $4 \times 10^8$  s  $^{-1}$ , each corresponding to yield strengths values of 6.220, 5.307, 4.702, and 4.347 GPa, respectively.

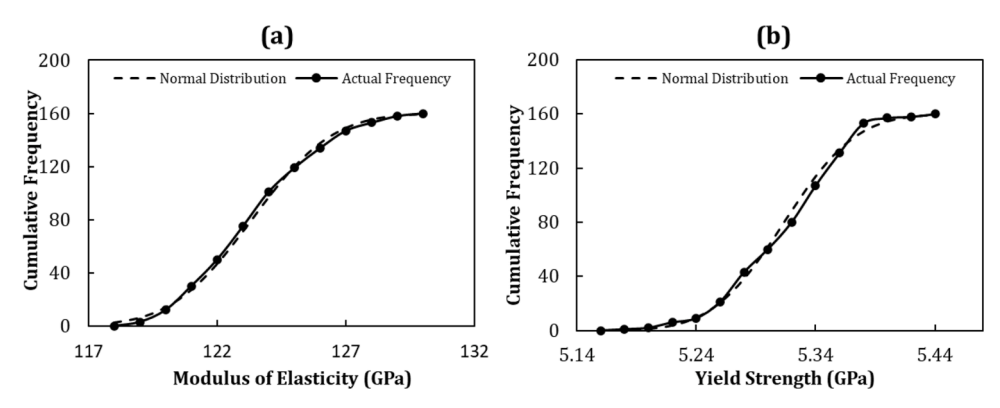


Fig. 4. Cumulative frequency distribution of simulated and curve fitted (a) elastic modulus and (b) yield strength of total 160 samples.

This resulted in a strain rate sensitivity of 13.459, illustrated in Fig. 5(a), which is subsequently employed to extrapolate the simulated yield points to the standard strain rate, assuming uniform sensitivity across all samples. The yield strengths at lower strain rates are then plotted to determine the mean and standard deviation using the cumulative normal distribution function. The investigation reveals a yield strength range between 504.173 and 529.457 MPa, with a mean and standard deviation of 518.516 and 4.611 MPa, respectively. Notably, Fig. 5(b) demonstrates a close alignment between the actual and cumulative Gaussian frequency curves.

$$\dot{\varepsilon} = A_c \ \sigma^{\frac{1}{m}} e^{\left(-\frac{E_d}{RT}\right)} \tag{10}$$

$$\ln(\dot{\varepsilon}) = \ln(A_c) + \frac{1}{m} \ln(\sigma) - \frac{E_a}{RT}$$
(11)

$$m = \frac{\partial \ln(\sigma)}{\partial \ln(\dot{\varepsilon})} = \frac{\ln(\sigma_2) - \ln(\sigma_1)}{\ln(\dot{\varepsilon}_2) - \ln(\dot{\varepsilon}_1)}$$
(12)

#### 3.2. Uncertainty of microstructural properties

The microstructural characteristics of a material are influenced by factors such as single-crystal properties, grain size, grain shape, and microstructural texture. In this particular investigation, the focus has been narrowed down to examining the impact of single-crystal properties and crystallographic texture on the microstructure, considering variations in both parameters. The uncertainty associated with singlecrystal properties is assessed using MD simulations (as reported in the previous section), while the uncertainty related to ODF values is derived from our prior research [3]; fluctuations of ~98 % ODF values are within 5 % from the mean values according to the corresponding experimental data. It is important to note that the uncertainty of all ODFs can be represented through a multivariate normal (Gaussian) distribution. Matrices representing single-crystal properties and their associated uncertainty, crucial for computing homogenized microstructural properties such as elastic modulus and yield strength, are derived using Eq. (9). The property matrix comprises a total of 50 elements for 50 independent nodal points modeled in Rodrigues orientation space. The mean values and variances for elastic modulus and yield strength are illustrated in Fig. 6 and Fig. 7, respectively. Upon incorporating the uncertainty propagation under the specified input conditions, the polycrystal elastic modulus exhibits mean and variance values of 167.281 GPa and 18.788 GPa<sup>2</sup>, respectively. This outcome suggests that approximately 98 % of the samples are within a 7.75 % range from the mean value; however, certain ODF values kept this percentage within 5.95 % as shown in Fig. 6(e). Conversely, yield strength is regarded as a linear property and can also be determined through the single-crystal properties of the material. Upon factoring in the uncertainty associated with the single-crystal yield strength matrix and ODF

values, the polycrystal demonstrates mean and variance values of 703.218 MPa and  $176.480~\text{MPa}^2$ , respectively. This outcome suggests that approximately 98 % of the samples are within a 5.65 % range from the mean value. However, when certain ODF values are considered, this percentage is reduced to 2.65 %, as depicted in Fig. 7(e). The overarching observation from these two propagation results is that the yield strength is more susceptible to the ODF uncertainty compared to elastic modulus.

# 3.3. Design of microstructures under uncertainty

In this section of the article, a few microstructure design studies are performed by considering the mean values  $(\mu_A)$  of ODFs and the covariance matrix entries  $(\Sigma_A)$  of ODFs as the design variables (x,y). Eq. (13) encompasses two property equations and two constraint equations, which are merely the expansion of Eq. (9) using associated matrix elements. These equations obtain the mean and variance values of properties, while the constraint equations focus on the volume normalization constraint to ensure that it has been satisfied under the effects of the uncertainty. This generalized set of equations is utilized for both elastic modulus and yield strength.

$$\mu_{Z} = \sum_{i=1}^{50} \mu_{P}(i)\mu_{A}(i)$$

$$\Sigma_{Z}^{2} = \sum_{i=1}^{50} \left[ \Sigma_{P}(i)\mu_{A}(i) \right]^{2} + \left[ \mu_{P}(i)\Sigma_{A}(i) \right]^{2} + \left[ \Sigma_{P}(i)\Sigma_{A}(i) \right]^{2}$$

$$1 = \sum_{i=1}^{50} Q(i)\mu_{A}(i)$$

$$0 = \sum_{i=1}^{50} \left[ Q(i)\Sigma_{A}(i) \right]^{2}$$

$$x = \mu_{A}(i)$$

$$y = \Sigma_{A}(i)$$
(13)

We considered four different cases: two cases for the maximization of the mean values of the properties and two cases for the minimization of the variance or standard deviation where a gradient-based optimization method has been employed in all cases. Additionally, the solved ODFs are plotted in three different pole figures using the method of Barton et al. [54], where the pole density function is  $P(h,y_i)$  at h plane unit normal and the location of  $y_1, y_2, \ldots, y_q$  for any specific diffraction plane on a unit sphere. The pole density function has been defined through the ODF  $(A_j)$  and the system matrix of  $(M_{ij})$  by  $\sum_{j=1}^k M_{ij} A_j$ , where k is the number of independent ODFs as defined earlier. Further, this definition of pole density function has been modified  $(P_i = P_i - M_{ik}/q_k)$  for the normalization constraint of unit volume fraction, which includes  $M_{ij} = M_{ij} - M_{ik}q_i/q_k$  for  $j = 1, 2, \ldots, (k-1)$ .

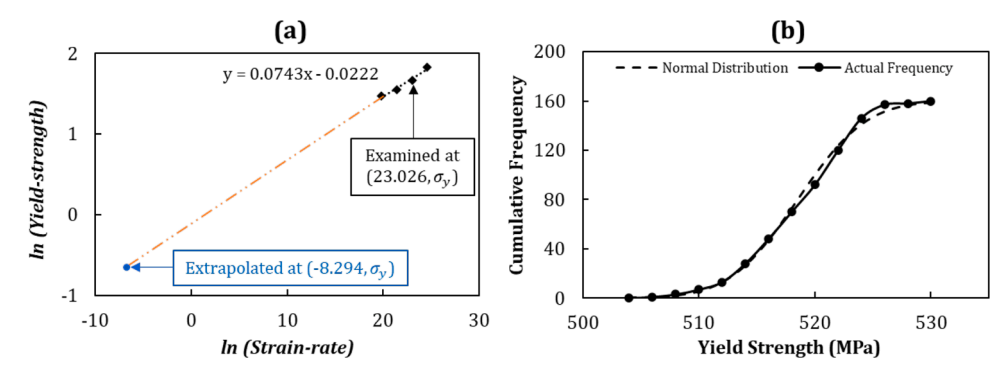


Fig. 5. (a) Determination of strain rate sensitivity from 4-different strain rate results and the method of scaling down the high strain rate yield strength and (b) cumulative frequency distribution of calculated and curve fitted yield strength at ASTM strain rate.

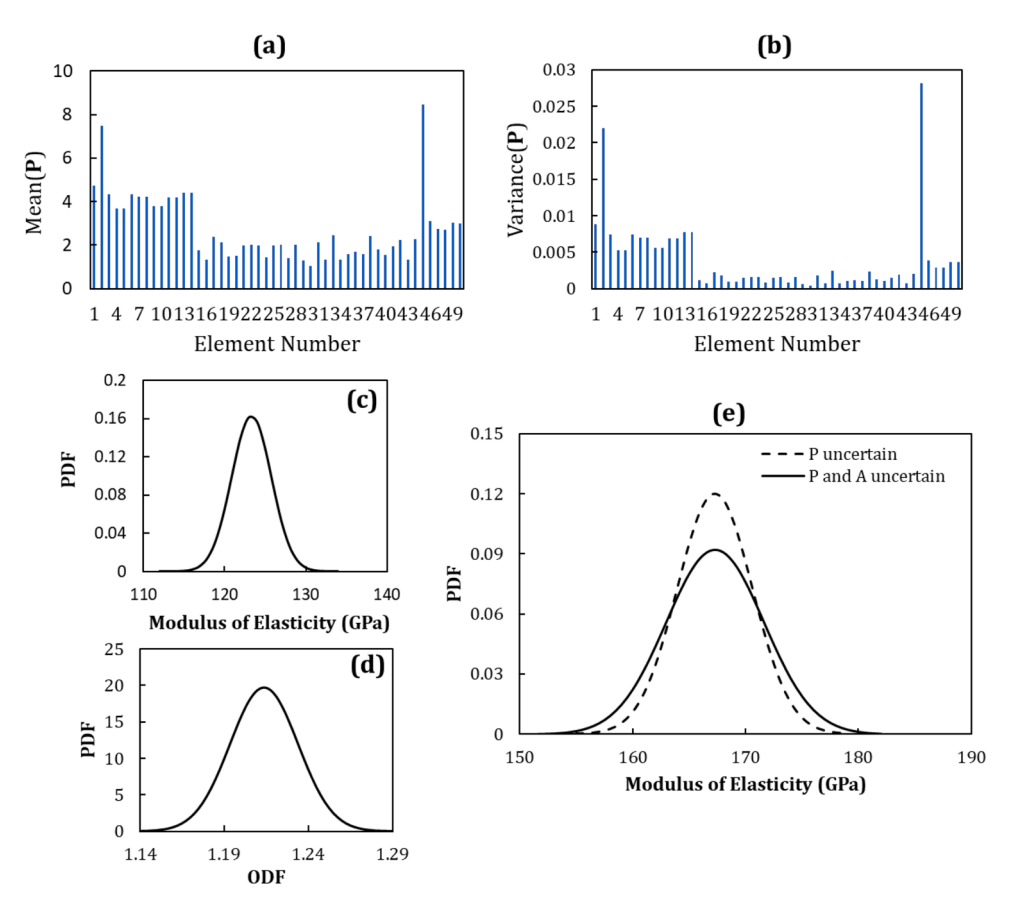


Fig. 6. (a) Mean, (b) variance of the elements of property matrix of elastic modulus; probability density of (c) single-crystal elastic modulus, (d) ODF, and (e) homogenized (meso-scale) elastic modulus of the microstructure.

# 3.3.1. Maximization of mean elastic modulus

The mean of the homogenized elastic modulus of the microstructure depends on the mean ODFs and the mean values of the elements of the property matrix owing to the linear relationship given in Eq. (9). In this case, the objective function is defined as, maximize  $\mu_E(\mu_A)$ . The mean of the ODFs have been considered as design variables and restricted through the volume normalization constraint. Next, the ODFs are assumed to vary  $\sim$ 5 % from mean values. This uncertainty leads to the probability density functions of the elastic modulus and yield strength illustrated in Fig. 8(a). The maximum objective function value of the mean elastic modulus is evaluated as 187.966 GPa and the associated yield strength for these optimized ODFs is computed as 785.203 MPa. On the other hand, the variances of elastic modulus and yield strength are obtained as 23.722 GPa² and 220.029 MPa², respectively. The optimized ODFs are shown in Rodrigues orientation space and through three different pole figures in Fig. 8(b) and (c), subsequently.

# 3.3.2. Minimization of variance of elastic modulus

The variance of the elastic modulus depends on several parameters, such as the mean and variance of ODFs and elements of the property matrix. This case considers both the mean and variance of ODFs as design variables to minimize the variance of elastic modulus, with an objective function given as,  $minimize~\Sigma_E(\mu_A,\Sigma_A)$ . The mean and variance of ODFs are required to satisfy the volume normalization constraints under uncertainty. In this case, the solved variance or standard deviation of each ODF tends to approach zero  $(\Sigma_A \to 0)$  because, otherwise, there is no optimum set of  $\Sigma_A$  that maximizes or minimizes the homogenized microstructure property, and these close-to-zero variances of ODFs can satisfy the constraints. The minimum objective function value for the variance of elastic modulus is 8.692 GPa^2 and the associated variance for yield strength is 31.211 MPa^2. On the other hand, the mean

of elastic modulus and yield strength are obtained as 148.619 GPa and 628.254 MPa, respectively. The probability densities of both mechanical properties for the optimized microstructure are shown in Fig. 9(a). The optimized ODFs are shown in Rodrigues orientation space and through three different pole figures in Fig. 9(b) and (c), subsequently.

## 3.3.3. Maximization of mean of yield strength

The mean value of homogenized yield strength is solely influenced by the mean values of ODFs and the elements of the property matrix. The present case deals with an objective function which is denoted as, maximize  $\mu_{\sigma_y}(\mu_A)$ . This design problem considers the mean ODFs as variables and has been constrained by the volume normalization equation. The ODFs are assumed to show approximately 5 % variations, leading to the probability densities for yield strength and elastic modulus depicted in Fig. 10(a). The maximum value of mean yield strength is obtained as 790.171 MPa, with an associated elastic modulus of 186.784 GPa. Conversely, the variances of yield strength and elastic modulus are determined as 222.822 MPa<sup>2</sup> and 23.427 GPa<sup>2</sup>, respectively. The optimized ODFs are visualized in Rodrigues orientation space through and three distinct pole figures in Fig. 10(b) and (c), subsequently.

# 3.3.4. Minimization of variance of yield strength

The variations of the yield strength are influenced by multiple parameters, including the mean values and variances of ODFs and the elements of the property matrix. In this scenario, both the mean values and variances of ODFs are treated as design variables to minimize the variance of yield strength given by the objective function, minimize  $\Sigma_{\sigma_y}(\mu_A, \Sigma_A)$ . The constraints on the mean and variance of ODFs are imposed through the volume normalization. In this specific case, the optimum variance or standard deviation of each ODF tends to approach

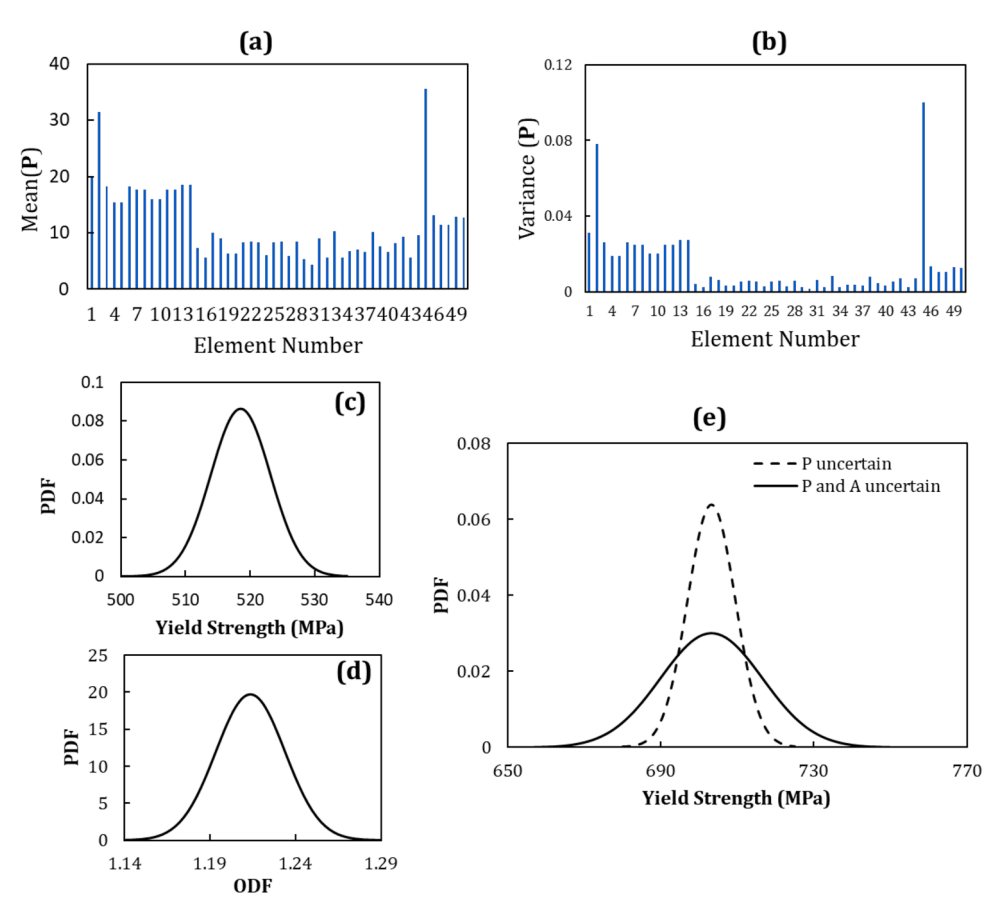


Fig. 7. (a) Mean, (b) variance of the elements of property matrix of yield strength; probability density of (c) single-crystal yield strength, (d) ODF, and (e) homogenized (meso-scale) elastic modulus of the microstructure.

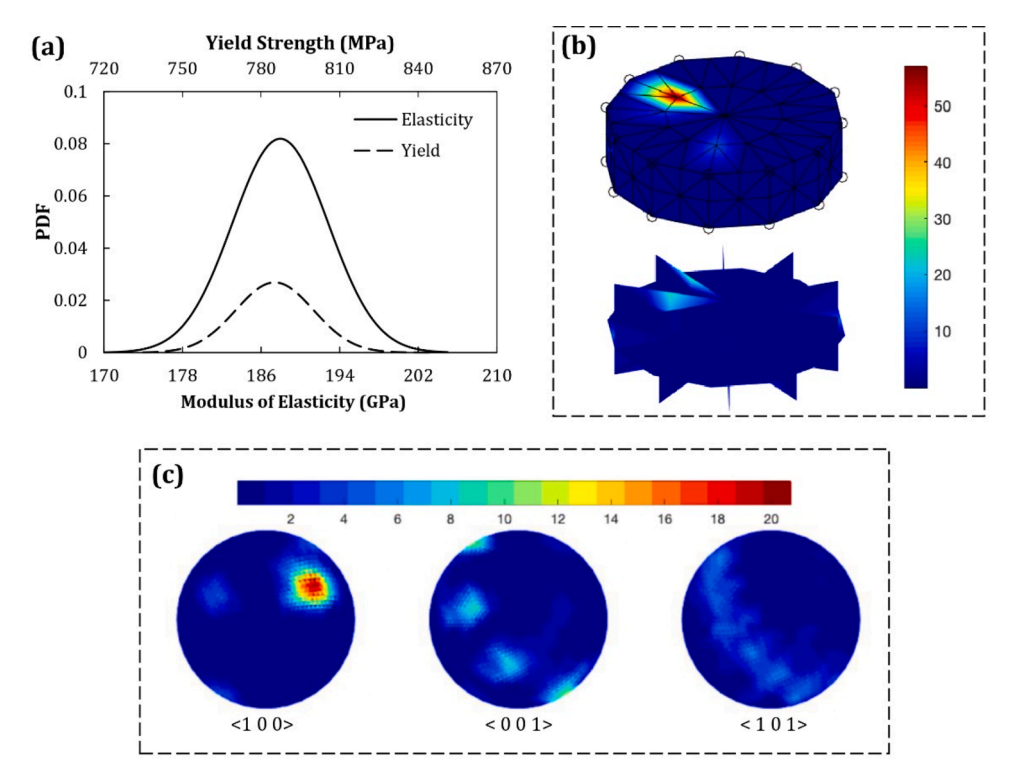


Fig. 8. (a) Probability density of the elastic modulus and yield strength for the microstructure design, maximizing the mean of homogenized elastic modulus. Representation of optimum ODFs in (b) Rodrigues orientation space and (c) through pole figures in  $\langle 1\ 0\ 0 \rangle$ ,  $\langle 0\ 0\ 1 \rangle$ , and  $\langle 1\ 0\ 1 \rangle$  directions.

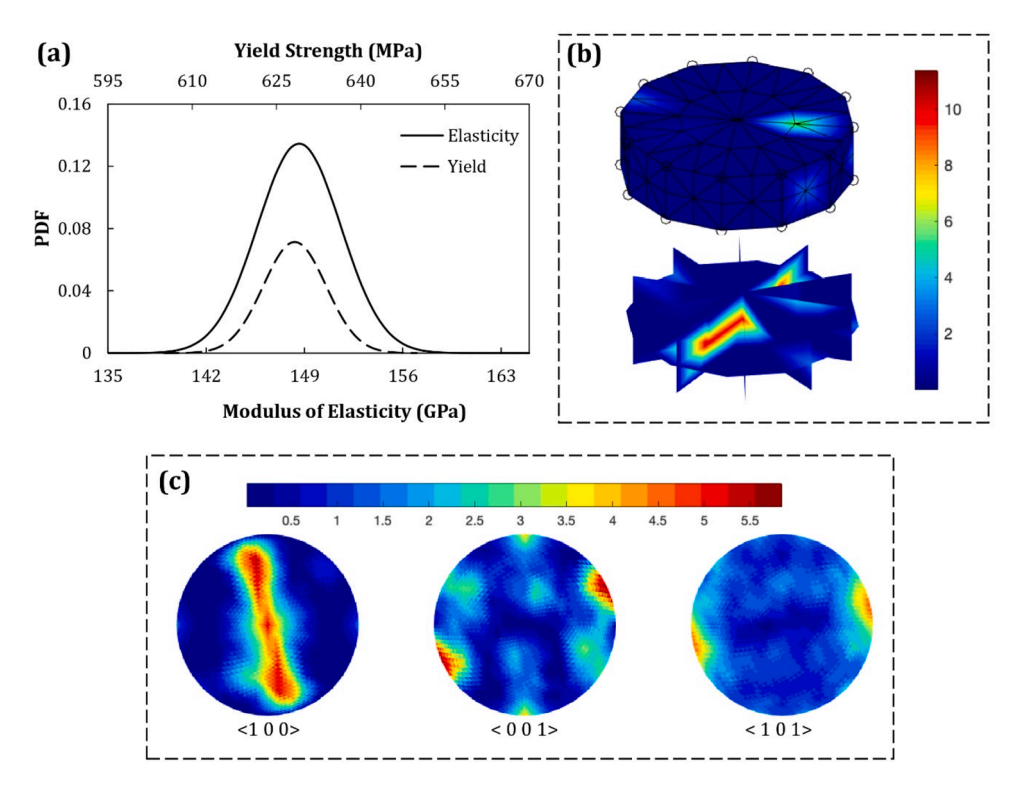


Fig. 9. (a) Probability density of the elastic modulus and yield strength for the microstructure design, minimizing the variance of homogenized elastic modulus. Representation of optimum ODFs in (b) Rodrigues orientation space and (c) through pole figures in  $\langle 1\ 0\ 0 \rangle$ ,  $\langle 0\ 0\ 1 \rangle$ , and  $\langle 1\ 0\ 1 \rangle$  directions.

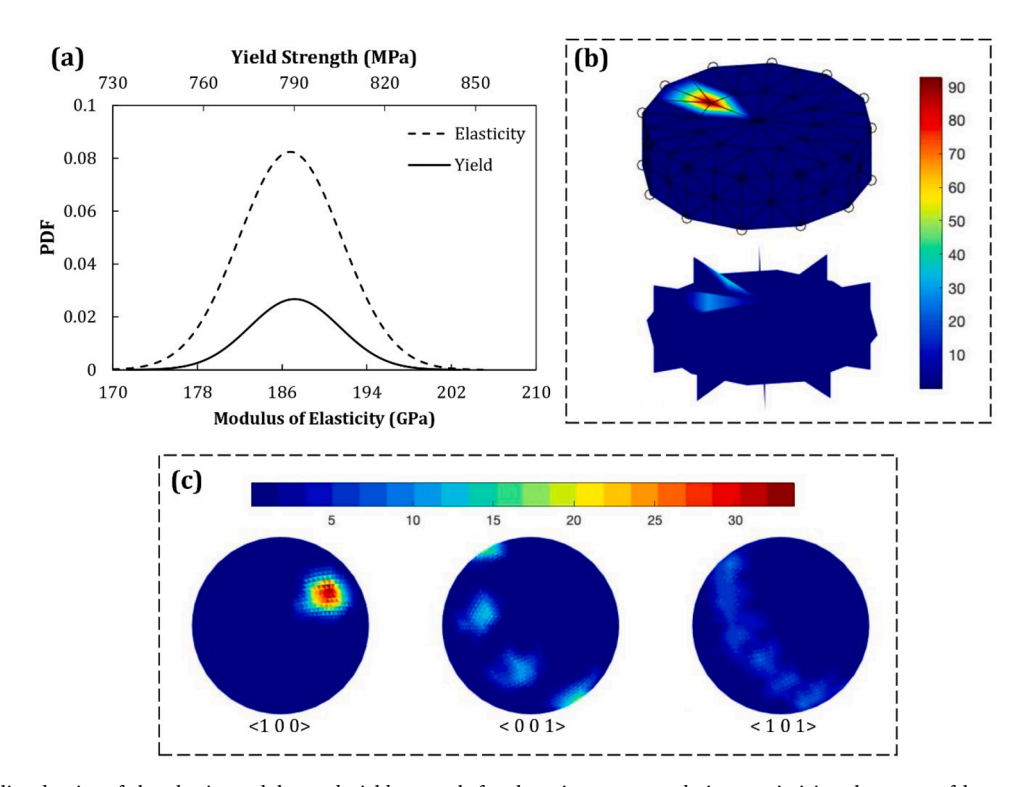


Fig. 10. (a) Probability density of the elastic modulus and yield strength for the microstructure design maximizing the mean of homogenized yield strength. Representation of optimum ODFs in (b) Rodrigues orientation space and (c) through pole figures in  $\langle 1\ 0\ 0 \rangle$ ,  $\langle 0\ 0\ 1 \rangle$ , and  $\langle 1\ 0\ 1 \rangle$  directions.

zero ( $\Sigma_A \rightarrow 0$ ). This is because there is no optimal set of  $\Sigma_A$  at larger values that maximize or minimize the homogenized property while satisfying the constraints. The minimum value for the variance of yield strength is determined as 30.865 MPa<sup>2</sup>, and the associated variance of elastic modulus is 8.789 GPa<sup>2</sup>. Conversely, the mean values of yield

strength and elastic modulus are obtained as 624.766 MPa and 149.159 GPa, respectively. The probability densities for the mechanical properties of the optimum microstructure design are illustrated in Fig. 11(a). The optimum ODFs are visually represented in Rodrigues orientation space, followed by their depiction through three distinct pole figures in

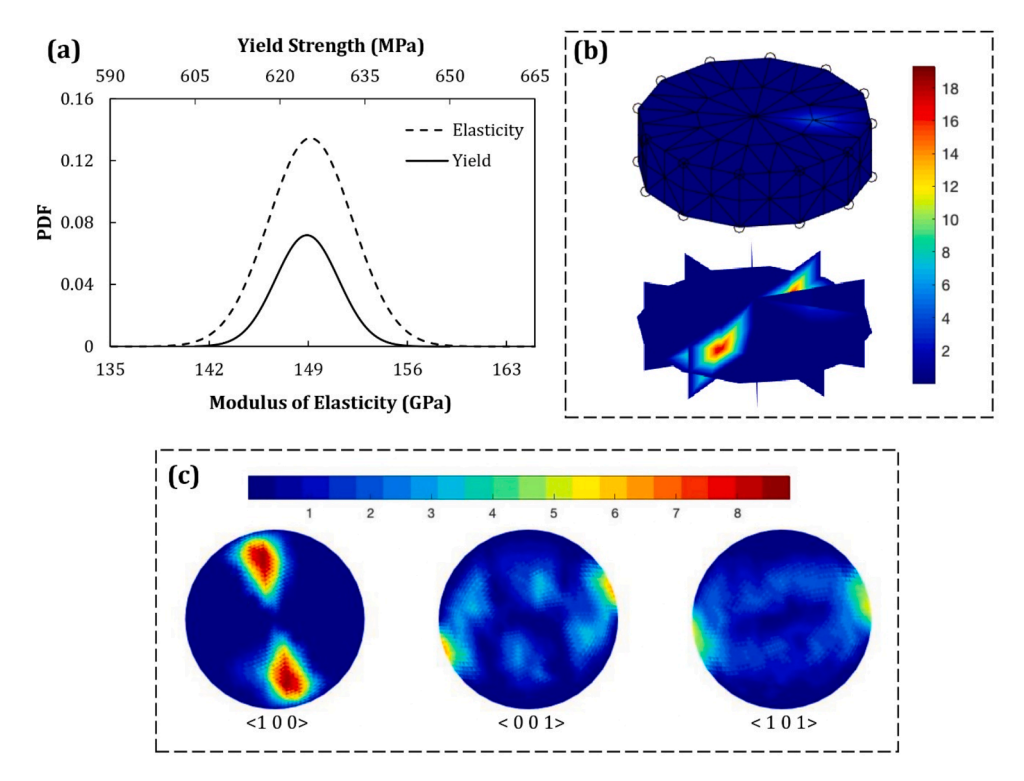


Fig. 11. (a) Probability density of the elastic modulus and yield strength for the microstructure design minimizing the variance of homogenized yield strength. Representation of optimum ODFs in (b) Rodrigues orientation space and (c) through pole figures in (1 0 0), (0 0 1), and (1 0 1) directions.

Fig. 11(b) and (c), respectively.

# 3.4. Transformation of non-linear parameters

This section discusses the computation of probability densities of parameters involving a non-linear relationship with elastic modulus, and thus with the ODFs and single-crystal properties. These parameters are divided into two types. Type-I includes the natural frequency of axial members, speed of sound in solid medium, critical length of columns which are directly proportional to the square root of the elastic modulus  $(\omega = g(E) = K \sqrt{E})$ . Type-II includes deflection and elongation/contraction of axial members which are inversely proportional to elastic modulus  $(\delta = g(E) = K/\sqrt{E})$  as shown in Fig. 12. The PDF of the homogenized elastic modulus of Ti-7Al has been stated in Eq. (14) where mean and standard deviation values of the optimum design maximizing elastic modulus are used. Later, this PDF is transformed to type-I  $(X=\omega)$  and type-II  $(X=\delta)$  scenarios by  $f_X(X) = f_E(h(X))|h'(X)|$  where  $h(X) = g^{-1}(X)$  and  $h'(X) = \frac{dh(X)}{dX}$ . The transformed PDF expression for type-I and

type-II parameters are stated in Eqs. (15) and (16), which show that the distributions of these two types of parameters are not Gaussian as their mother distribution. As shown by the probability densities plotted in Fig. (13), the higher values of (13) exhibit higher uncertainty in these parameters.

$$f_E(E) = \frac{1}{\sigma\sqrt{2\pi}} e^{-\frac{1}{2}\left(\frac{E-\mu}{\sigma}\right)^2}$$
 (14)

$$f_{\omega}(\omega) = \frac{2\omega}{K^{2}\sigma_{F}\sqrt{2\pi}} e^{-\frac{1}{2}\left(\frac{\omega^{2}}{\frac{K^{2}}{\sigma_{E}}} - \mu_{E}}{\sigma_{E}}\right)^{2}}$$

$$(15)$$

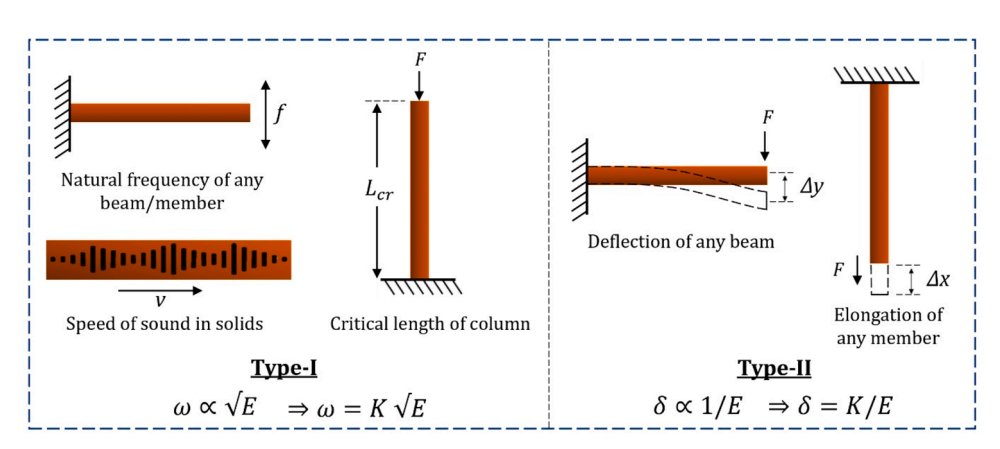


Fig. 12. A few examples for the selected two types of non-linear properties/parameters.

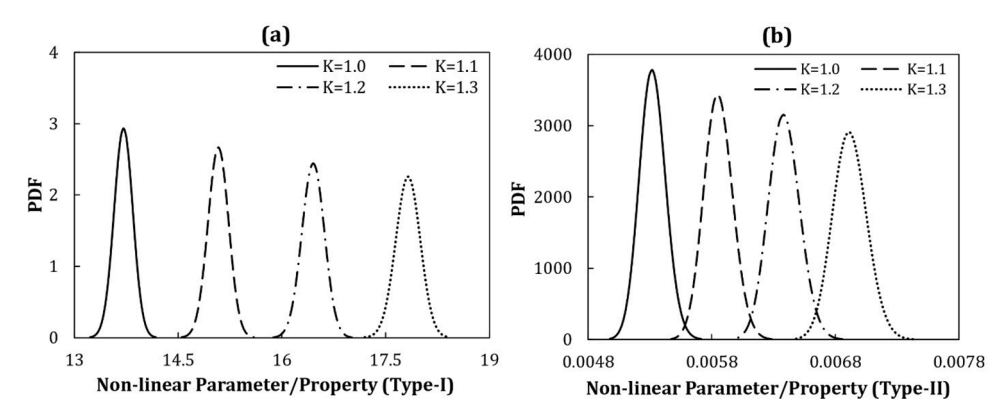


Fig. 13. Transformed PDF of (a) type-I, (a) type-II parameter/property for different K values.

$$f_{\delta}(\delta) = \frac{K}{\delta^2 \sigma_E \sqrt{2\pi}} e^{-\frac{1}{2} \left(\frac{K}{\delta} - \mu_E}{\sigma_E}\right)^2}$$
(16)

#### 4. Conclusions

This study investigates how variations associated with the randomness of substitutional atoms and the uncertainty of microstructural texture affect meso-scale mechanical properties. Using an analytical UQ method, we identify microstructural texture designs for optimum mechanical performance under these variations. Comprehensive conclusions can be drawn by several key insights:

- a) The frequency distribution analysis reveals that the elastic modulus and yield strength of single-crystal Ti-7Al exhibit deviations of 4.55 % and 2.40 %, respectively from their mean values, conforming closely to a Gaussian distribution. Notably, the recalculated yield strength at standard strain rates shows similar distribution pattern, as it has been linearly extrapolated from the strain rate sensitivity results.
- b) The homogenized polycrystal properties vary less than 8 % from their corresponding mean values. The yield strength is more vulnerable to the texture uncertainty compared to elastic modulus.
- c) In the case of maximizing mean (expected) values of properties, only a few independent ODFs have non-zero values, which shows that the optimum microstructures correspond to sharp textures.
- d) On the contrary, the minimization of the variance of properties leads to microstructure designs with higher number of non-zero independent ODFs. However, this occurs at the cost of lower expected values, nearing the lowest feasible values.
- e) The PDFs of the properties/parameters which have non-linear relationships with elastic modulus do not follow a normal distribution as expected. Nonetheless, these results offered valuable insights into the distributions of any properties/parameters which are reliant on mechanical properties of interest.

# CRediT authorship contribution statement

**Md Maruf Billah:** Conceptualization, Data curation, Methodology, Validation, Writing – original draft, Writing – review & editing. **Pinar Acar:** Funding acquisition, Methodology, Project administration, Supervision, Writing – original draft, Writing – review & editing.

# Declaration of competing interest

The authors declare that they have no known competing financial interests or personal relationships that could have appeared to influence the work reported in this paper.

# Acknowledgements

The authors would like to acknowledge the financial support from the National Science Foundation (NSF) CMMI Award #2053840 (PD: Dr. Kathryn Jablokow).

# Supplementary materials

Supplementary material associated with this article can be found, in the online version, at doi:10.1016/j.actamat.2024.119879.

#### References

- S. Wan, R.C. Sinclair, P.V. Coveney, Uncertainty quantification in classical molecular dynamics, Phil. Trans. R. Soc. A. 379 (2197) (2021) 20200082, https://doi.org/10.1098/rsta.2020.0082 rsta.2020.0082May.
- [2] J. Allison, D. Backman, L. Christodoulou, Integrated computational materials engineering: a new paradigm for the global materials profession, JOM 58 (11) (2006) 25–27, https://doi.org/10.1007/s11837-006-0223-5. Nov.
- [3] P. Acar, V. Sundararaghavan, Uncertainty quantification of microstructural properties due to variability in measured pole figures, Acta Mater. 124 (2017) 100–108, https://doi.org/10.1016/j.actamat.2016.10.070. Feb.
- [4] P.J. Madrid, D. Sulsky, R.A. Lebensohn, Uncertainty quantification in prediction of the in-plane young's modulus of thin films with fiber texture, J. Microelectromech. Syst. 23 (2) (2014) 380–390, https://doi.org/10.1109/JMEMS.2013.2279500. Apr.
- [5] A. Creuziger, K. Syed, T. Gnäupel-Herold, Measurement of uncertainty in orientation distribution function calculations, SCR Mater. 72–73 (2014) 55–58, https://doi.org/10.1016/j.scriptamat.2013.10.017. Feb.
- [6] J. Luan, G. Liu, H. Wang, A. Ullah, On the sampling of three-dimensional polycrystalline microstructures for distribution determination, J. Microsc. 244 (2) (2011) 214–222. https://doi.org/10.1111/j.1365-2818.2011.03531.x.
- [7] B. Hiriyur, H. Waisman, G. Deodatis, Uncertainty quantification in homogenization of heterogeneous microstructures modeled by XFEM, Int. J. Numer. Methods Eng. 88 (3) (2011) 257–278. https://doi.org/10.1002/nme.3174.
- [8] S. Sakata, F. Ashida, T. Kojima, M. Zako, Three-dimensional stochastic analysis using a perturbation-based homogenization method for elastic properties of composite material considering microscopic uncertainty, Int. J. Solids Struct. 45 (3) (2008) 894–907. https://doi.org/10.1016/j.ijsolstr.2007.09.008. Feb.
- [9] B. Kouchmeshky, N. Zabaras, The effect of multiple sources of uncertainty on the convex hull of material properties of polycrystals, Comput. Mater. Sci. 47 (2) (2009) 342–352, https://doi.org/10.1016/j.commatsci.2009.08.010. Dec.
- [10] S. Sakata, F. Ashida, M. Zako, Kriging-based approximate stochastic homogenization analysis for composite materials, Comput. Methods Appl. Mech. Eng. 197 (21) (2008) 1953–1964, https://doi.org/10.1016/j.cma.2007.12.011. Apr
- [11] A. Clément, C. Soize, J. Yvonnet, Computational nonlinear stochastic homogenization using a nonconcurrent multiscale approach for hyperelastic heterogeneous microstructures analysis, Int. J. Numer. Methods Eng. 91 (8) (2012) 799–824, https://doi.org/10.1002/nme.4293.
- [12] A. Clément, C. Soize, J. Yvonnet, Uncertainty quantification in computational stochastic multiscale analysis of nonlinear elastic materials, Comput. Methods Appl. Mech. Eng. 254 (2013) 61–82, https://doi.org/10.1016/j.cma.2012.10.016. Feb.
- [13] A. Radecka, J. Coakley, I.P. Jones, D. Rugg, T.C. Lindley, D. Dye, Ordering and the micromechanics of Ti–7Al, Mater. Sci. Eng. A 650 (2016) 28–37, https://doi.org/ 10.1016/j.msea.2015.09.070. Jan.
- [14] R.R. Boyer, Attributes, characteristics, and applications of titanium and its alloys, JOM 62 (5) (2010) 21–24, https://doi.org/10.1007/s11837-010-0071-1. May.

- [15] D. Banerjee, J.C. Williams, Perspectives on titanium science and technology, Acta Mater. 61 (3) (2013) 844–879, https://doi.org/10.1016/j.actamat.2012.10.043. Feb.
- [16] C. Leyens, M. Peters (Eds.), Titanium and Titanium Alloys: Fundamentals and Applications, 1st ed., Wiley, 2003 https://doi.org/10.1002/3527602119.
- [17] F.P.E. Dunne, D. Rugg, A. Walker, Lengthscale-dependent, elastically anisotropic, physically-based hcp crystal plasticity: application to cold-dwell fatigue in Ti alloys, Int. J. Plast. 23 (6) (2007) 1061–1083, https://doi.org/10.1016/j.iiplas.2006.10.013. Jun.
- [18] F.F. Worsnop, S.L.M. Lea, J. Ilavsky, D. Rugg, D. Dye, Crystallographic ordering of Al and Sn in α-Ti, SCR Mater. 226 (2023) 115221, https://doi.org/10.1016/j. scriptamat.2022.115221. Mar.
- [19] J. Ding, et al., Multi-scale numerical simulation of fracture behavior of nickelaluminum alloy by coupled molecular dynamics and cohesive finite element method (CFEM), Theor. Appl. Fract. Mech. 109 (2020) 102735, https://doi.org/ 10.1016/j.tafmec.2020.102735. Oct.
- [20] P. Acar, Uncertainty quantification for Ti-7Al alloy microstructure with an inverse analytical model (AUQLin), Materials 12 (11) (2019) 11, https://doi.org/10.3390/ ma12111773. Art. no.Jan.
- [21] P. Acar, A. Ramazani, V. Sundararaghavan, Crystal plasticity modeling and experimental validation with an orientation distribution function for Ti-7Al alloy, Metals 7 (11) (2017) 11, https://doi.org/10.3390/met7110459. Art. no.Nov.
- [22] P. Acar, 'Design Optimization of Metallic Alloy Microstructures under Epistemic Uncertainty', in AIAA Scitech 2020 Forum, American Institute of Aeronautics and Astronautics. 10.2514/6.2020-0884.
- [23] A. Tran, P. Robbe, H. Lim, Multi-fidelity microstructure-induced uncertainty quantification by advanced Monte Carlo methods, Materialia 27 (2023) 101705, https://doi.org/10.1016/j.mtla.2023.101705. Mar.
- [24] D. Thillaithevan, P.J. Bruce, M.J. Santer, Modelling material uncertainty in multiscale optimization using lattice microstructures. AIAA Scitech 2021 Forum, VIRTUAL EVENT: American Institute of Aeronautics and Astronautics, 2021, https://doi.org/10.2514/6.2021-1593. Jan.
- [25] J. von Pezold, A. Dick, M. Friák, J. Neugebauer, Generation and performance of special quasirandom structures for studying the elastic properties of random alloys: application to Al-Ti, Phys. Rev. B 81 (9) (2010) 094203, https://doi.org/10.1103/ PhysRevB.81.094203. Mar.
- [26] L. Zhang, Y. Xiang, J. Han, D.J. Srolovitz, The effect of randomness on the strength of high-entropy alloys, Acta Mater. 166 (2019) 424–434, https://doi.org/10.1016/ i.actamat.2018.12.032. Mar.
- [27] V. Popescu, A. Zunger, Effective Band Structure of Random Alloys, Phys. Rev. Lett. 104 (23) (2010) 236403. https://doi.org/10.1103/PhysRevLett.104.236403. Jun.
- [28] R.E. Lim, D.C. Pagan, D.E. Boyce, J.V. Bernier, P.A. Shade, A.D. Rollett, Grain-resolved temperature-dependent anisotropy in hexagonal Ti-7Al revealed by synchrotron X-ray diffraction, Mater. Charact. 174 (2021) 110943, https://doi.org/10.1016/j.matchar.2021.110943. Apr.
- [29] Y.K. Kim, H.K. Kim, W.S. Jung, B.J. Lee, Atomistic modeling of the Ti–Al binary system, Comput. Mater. Sci. 119 (2016) 1–8, https://doi.org/10.1016/j. commatsci.2016.03.038, Jun.
- [30] Md.M. Billah, M.S. Rabbi, K.A. Rahman, P. Acar, Temperature and strain rate dependent tensile properties of titanium carbide/nitride MXenes, Mater. Chem. Phys. 312 (2024) 128581, https://doi.org/10.1016/j.matchemphys.2023.128581. Jan.
- [31] Md.M. Billah, R.I. Siddiquee, M. Motalab, R. Paul, M.S. Rabbi, Effects of temperature and strain rate on tensile properties of (Ag,Cu)-Sn intermetallic compounds: a molecular dynamics study, J. Mater. Res. Technol. 18 (2022) 3044–3055, https://doi.org/10.1016/j.jmrt.2022.03.141. May.
- [32] Md.M. Billah, A.R. Aad, S. Das, M. Motalab, R. Paul, Dependence of mechanical and thermal deformation behaviors on crystal size and direction of Cu3Sn intermetallic: a molecular dynamics study, Alexandria Eng. J. 66 (2023) 79–96, https://doi.org/10.1016/j.aej.2022.11.025. Mar.
- [33] Md.M. Billah, S. Das, A.R. Aad, R. Paul, Tensile properties dependency on crystal size and direction of single crystal Ag3Sn intermetallic compound: a molecular dynamics study, J. Mater. Res. Technol. 20 (Sep. 2022) 2094–2108, https://doi. org/10.1016/j.jmrt.2022.07.188.

- [34] M.M. Billah, R.I. Siddiquee, and M. Motalab, 'Temperature dependent mechanical properties of inter-metallic compounds in nano-solder joints', 2019, Accessed: Jan. 08, 2024. [Online]. Available: https://www.academia.edu/download/94681 778./1 pdf
- [35] A.K. Subramaniyan, C.T. Sun, Continuum interpretation of virial stress in molecular simulations, Int. J. Solids Struct. 45 (14) (2008) 4340–4346, https://doi. org/10.1016/j.ijsolstr.2008.03.016. Jul.
- [36] V. Sundararaghavan, N. Zabaras, Linear analysis of texture–property relationships using process-based representations of Rodrigues space, Acta Mater. 55 (5) (2007) 1573–1587, https://doi.org/10.1016/j.actamat.2006.10.019. Mar.
- [37] A. Heinz, P. Neumann, Representation of orientation and disorientation data for cubic, hexagonal, tetragonal and orthorhombic crystals, Acta Cryst. A 47 (6) (1991) 780–789, https://doi.org/10.1107/S0108767391006864. Nov.
- [38] A. Kumar, P.R. Dawson, Computational modeling of f.c.c. deformation textures over Rodrigues' space, Acta Mater. 48 (10) (2000) 2719–2736, https://doi.org/ 10.1016/S1359-6454(00)00044-6. Jun.
- [39] J.H. Cho, Determination of volume fraction of the texture components in the Rodrigues fundamental region, Mater. Sci. Eng. A 465 (1) (2007) 228–237, https://doi.org/10.1016/j.msea.2007.03.030. Sep.
- [40] H.J. Bunge, Texture Analysis in Materials Science, .., Butterworth Publishers, London, 1982.
- [41] M. Francois, J.M. Sprauel, J.L. Lebrun, Construction of a pseudo-material representative of a real textured material from ODF or direct pole figures, Texture, Stress Microstruct. 14 (1991) 169–174.
- [42] P.V. Houtte, On the representation of texture functions of cubic metals in Euler space, Textures Microstruct. 7 (1970). Accessed: Jan. 09, 2024. [Online]. Available: https://downloads.hindawi.com/archive/1987/321546.pdf.
- [43] J.H. Cho, A.D. Rollett, K.H. Oh, Determination of volume fractions of texture components with standard distributions in euler space, Metall. Mater. Trans. A 35 (3) (Mar. 2004) 1075–1086, https://doi.org/10.1007/s11661-004-0033-8.
- [44] A. Kumar, P.R. Dawson, Modeling crystallographic texture evolution with finite elements over neo-Eulerian orientation spaces, Comput. Methods Appl. Mech. Eng. 153 (3) (1998) 259–302, https://doi.org/10.1016/S0045-7825(97)00072-8. Jan.
- [45] P. Acar, V. Sundararaghavan, Linear solution scheme for microstructure design with process constraints, AIAA J. 54 (12) (2016) 4022–4031, https://doi.org/ 10.2514/1.J055247.
- [46] P. Acar, V. Sundararaghavan, Reduced-Order modeling approach for materials design with a sequence of processes, AIAA J. 56 (12) (2018) 5041–5044, https://doi.org/10.2514/1.J057221.
- [47] P. Acar, V. Sundararaghavan, Uncertainty quantification of microstructural properties due to experimental variations, AIAA J. 55 (8) (2017) 2824–2832, https://doi.org/10.2514/1.J055689.
- [48] P. Acar, Eliminating mesh sensitivities in microstructure design with an adjoint algorithm, Finite Elem. Anal. Des. 154 (2019) 22–29, https://doi.org/10.1016/j. finel.2018.10.001, Feb.
- [49] P. Acar, V. Sundararaghavan, M.D. Graef, Computational modeling of crystallographic texture evolution over cubochoric space, Modelling Simul. Mater. Sci. Eng. 26 (6) (2018) 065012, https://doi.org/10.1088/1361-651X/aad20b. Aug.
- [50] Ş. Çallıoğlu, P. Acar, Design of β-Titanium microstructures for implant materials, Mater. Sci. Eng. C 110 (2020) 110715, https://doi.org/10.1016/j. msec.2020.110715. May.
- [51] P. Acar, Machine learning reinforced crystal plasticity modeling under experimental uncertainty, AIAA J. 58 (8) (2020) 3569–3576, https://doi.org/ 10.2514/1.J059233.
- [52] M. Hasan, P. Acar, Machine learning reinforced microstructure-sensitive prediction of material property closures, Comput. Mater. Sci. 210 (2022) 110930, https://doi. org/10.1016/j.compatsci.2021.110930. Jul
- [53] M.Q. Chen, S.S. Quek, Z.D. Sha, C.H. Chiu, Q.X. Pei, Y.W. Zhang, Effects of grain size, temperature and strain rate on the mechanical properties of polycrystalline graphene – A molecular dynamics study, Carbon 85 (2015) 135–146, https://doi. org/10.1016/j.carbon.2014.12.092. Apr.
- [54] N.R. Barton, D.E. Boyce, P.R. Dawson, Pole figure inversion using finite elements over rodrigues space, Textures Microstruct. 35 (2) (2002) 113–144, https://doi. org/10.1080/073033002100000182. Jan.